

Deep Learning of Force Manifolds from the Simulated Physics of Robotic Paper Folding

Dezhong Tong^{*,1}, Andrew Choi^{*,2}, Demetri Terzopoulos², Jungseock Joo³, and Mohammad Khalid Jawed^{†,1}

Abstract—Robotic manipulation of slender objects is challenging, especially when the induced deformations are large and nonlinear. Traditionally, learning-based control approaches, e.g., imitation learning, have been used to tackle deformable material manipulation. Such approaches lack generality and often suffer critical failure from a simple switch of material, geometric, and/or environmental (e.g., friction) properties. In this article, we address a fundamental but difficult step of robotic origami: forming a predefined fold in paper with only a single manipulator. A data-driven framework combining physically-accurate simulation and machine learning is used to train deep neural network models capable of predicting the external forces induced on the paper given a grasp position. We frame the problem using scaling analysis, resulting in a control framework robust against material and geometric changes. Path planning is carried out over the generated manifold to produce robot manipulation trajectories optimized to prevent sliding. Furthermore, the inference speed of the trained model enables the incorporation of real-time visual feedback to achieve closed-loop sensorimotor control. Real-world experiments demonstrate that our framework can greatly improve robotic manipulation performance compared against natural paper folding strategies, even when manipulating paper objects of various materials and shapes.

Index Terms—robotic manipulation, deformable material manipulation, deep neural networks, data-driven models, closed-loop sensorimotor control

I. INTRODUCTION

From shoelaces to clothes, we encounter flexible slender structures throughout our everyday lives. These structures are often characterized by their ability to undergo large deformations when subjected even to moderate forces, such as gravity. People possess an incredible innate understanding of the dynamics of such deformable objects; e.g., we can use gravity to perfectly manipulate a shirt over our heads. Instilling such intuition into robots remains an important research problem and has the potential to breed numerous applications with considerable economic and humanitarian potential. Some examples include preparing deformable products in the food industry [1], [2], assisting in the medical field [3]–[5], and providing caregiving assistance to elderly and disabled communities, including with respect to dressing [6]–[10] and feeding [11], [12]. However, the

The authors are with the University of California, Los Angeles (UCLA), CA 90095, USA.

¹Dezhong Tong and M. Khalid Jawed are with the UCLA Department of Mechanical & Aerospace Engineering (email: tlt960308@g.ucla.edu; khalidjm@seas.ucla.edu).

²Andrew Choi and Demetri Terzopoulos are with the UCLA Computer Science Department (email: asjchoi@cs.ucla.edu; dt@cs.ucla.edu).

³Jungseock Joo is with the UCLA Department of Communication and is currently working at NVIDIA Corporation (email: jjoo@comm.ucla.edu).

* Equal contribution.

† Corresponding author.

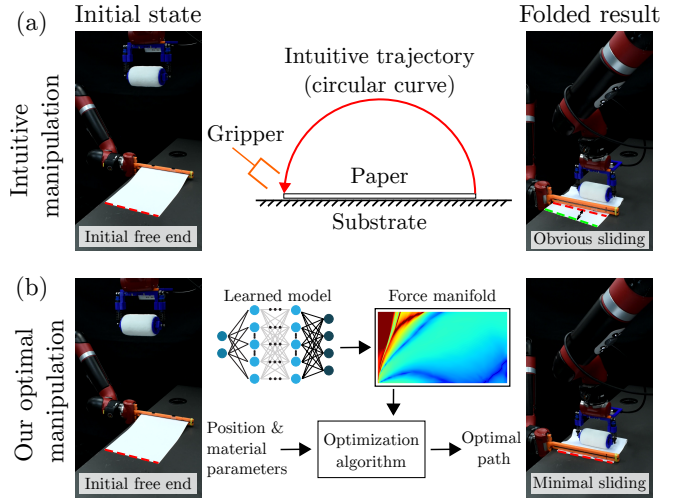


Fig. 1. Half valley folding for A4 paper with (a) intuitive manipulation and (b) our designed optimal manipulation. An intuitive manipulation scheme such as tracing a semi-circle experiences significant sliding due to the bending stiffness of the paper, resulting in a poor fold. By contrast, our optimal manipulation approach achieves an excellent fold by taking into consideration the paper’s deformation and thus minimizing sliding.

robotic manipulation of deformable objects is highly nontrivial as a robot must be able to take into account future deformations of the manipulated object to complete manipulation tasks successfully.

Prior research has focused primarily on manipulating either cloth [13]–[18] or ropes [12], [19]–[25] and as a result, the robotic manipulation of many other deformable objects still lacks robust solutions. In this article, we address a particularly difficult deformable manipulation task — folding paper. Paper is similar to cloth but typically has a much larger bending stiffness and a slippery surface. Therefore, compared with folding garments and fabrics, more delicate and insightful manipulations are required for folding sheets of paper.

A. Our Approach

We propose a framework that combines physically accurate simulation, scaling analysis, and machine learning to generate folding trajectories optimized to prevent sliding. With scaling analysis, we make the problem non-dimensional, resulting in both dimensionality reduction and generality. We then train neural networks, whose outputs are referred to as neural force manifolds (NFM), to continuously approximate a scaled force manifold sampled purely from simulation. Compared to numerical models that require the entire geometric configuration

of the paper, NFM maps the external forces of the paper given only the grasp position. Therefore, we can generate trajectories optimized to minimize forces (and thus minimize sliding) by applying path planning algorithms in near real-time. We show that our approach is capable of folding paper on extremely slick surfaces with little-to-no sliding (Fig. 1(b)).

Our main contributions are as follows: (1) we formulate a solution to the folding problem in a physically robust manner using scaling analysis, resulting in complete generality with respect to material, geometric, and environmental properties; (2) we train a neural network with non-dimensional simulation data forming a fast and accurate model that can generate a descriptive force manifold for trajectory optimization; (3) we utilize the high inference speed of our trained model with a perception system to construct a robust and efficient closed-loop sensorimotor control algorithm for the folding task, and finally (4) we demonstrate full sim2real realization through an extensive robotic case study featuring 210 experiments across paper sheets of various materials and shapes. While several previous works have trained their policies purely from simulation data [7], [19], [26]–[28], these works lacked real world validation. To our knowledge, our framework is the first to provide optimal folding trajectories with complete generality.

We release supplementary videos as well as all source code and CAD files as open source at <https://github.com/StructuresComp/deep-robotic-paper-folding>.

B. Overview

The remainder of the article is organized as follows: We begin with a review of related work in Sec. II. A brief description of the folding problem is presented in Sec. III. The formulation of a reduced-order physics-based model is discussed in Sec. IV, where we formulate the folding problem using scaling analysis. In Sec. V, we formulate our learning framework as well as algorithms for optimal path planning. Next, in Sec. VI, we introduce our robotic system as well as formulate our closed-loop visual feedback pipeline. Experimental results for a robot case study and analysis of the results are given in Sec. VII. Finally, we provide concluding remarks and discuss the potential of future research avenues in Sec. VIII.

II. RELATED WORK

The majority of prior works tackling the folding problem can be roughly divided into four categories: mechanical design-based solutions, vision-based solutions, learning-based solutions, and model-based solutions.

Mechanical design-based approaches typically involve solving the folding problem through highly specialized manipulators or end effectors. Early approaches involve specialized punches and dies for sheet metal bending [29]. More recently, highly specialized manipulators for robotic origami folding have also been developed [30]. Such methods can reliably produce repeatable folding but are often limited to a highly specific fold, geometry, and/or material.

Vision-based approaches involve folding deformable materials by generating folding motions purely from visual input.

These approaches are usually common for folding clothes [14], [16], [31] as they are extremely soft, which results in the easy predictability of their deformation state given a particular action. Such approaches can be effective and rather simple to implement, but do not transfer well to paper folding as paper possesses a much higher stiffness when compared to fabric and will attempt to restore its natural, undeformed state if not properly handled.

Learning-based approaches involve the robot learning how to fold through training data. The most popular has been to learn control policies from human demonstrations, also known as learning from demonstrations (LfD). Prior research has demonstrated flattening and folding towels [32], [33]. Teleop demonstrations are a popular avenue for training policies and have been used to learn how to manipulate deformable linear objects (DLOs) [34] as well as folding fabric [35]. To eliminate the need for expensive human-labeled data, researchers have also focused on tackling the sim2real problem for robotic folding, where reinforcement learning has been used to train robots to fold fabrics and cloths completely from simulation [26], [28], [36]. More recently, Zheng et al. [37] used reinforcement learning to train a robot to flip pages in a binder through tactile feedback. Pure learning-based methods have shown promising performance, but only for specific tasks whose state distribution matches the training data. Such methods tend to generalize quite poorly; e.g., when the material or geometric properties change drastically.

Model-based approaches, where the model can either be known or learned, often use model predictive control to manipulate the deformable object. They involve learning the natural dynamics of deformable objects through random perturbations [38]. These models are generally fast, but they can be inaccurate when experiencing new states. Known models are often formulated to be as physically accurate as possible. They can be referred to as physics-based (as opposed to simulated). Their physical accuracy allows for the direct application of their predictive capabilities in the real world. Examples are published for rectangular cloth folding [39], strip folding [40], and garment folding [41]. Still, known models are usually quite expensive to run and must often face a trade-off between accuracy and efficiency.

Despite the large quantity of prior research focusing on 2D deformable object manipulation, the majority of these efforts have limited their scope to soft materials such as towels and cloth. Such materials are highly compliant and often do not exhibit complicated nonlinear deformations, thus allowing for solutions lacking physical insight. We instead tackle the scenario of folding papers of various stiffnesses with a single manipulator. Because of its relatively high bending stiffness and slippery surface, paper is significantly more difficult to manipulate since large deformations will cause sliding of the paper on the substrate. Such an example can be observed in Fig. 1(a), where intuitive folding trajectories that may work on towels and cloth fail for paper due to undesired sliding.

However, a few works have attempted to solve the paper folding problem. For example, Elbrechter et al. [42] demonstrated paper folding using visual tracking and real-time physics-based modeling with impressive results, but they required expensive

end effectors (two Shadow Dexterous Hands), one end effector to hold the paper down while folding at all times, and the paper to have AR tags for visual tracking. Similarly, Namiki et al. [43] also achieved paper folding through dynamic motion primitives and used physics-based simulations to estimate the deformation of the paper sheet, also requiring highly specialized manipulators and an end effector to hold the paper down while folding. By contrast, our method can fold papers reliably without any need for holding down the paper during the folding operation and requires only an extremely simple 3D printed gripper. Other approaches have also attempted to fold with a single manipulator while minimizing sliding [36], [40], but these methods focused on fabrics whose ends were taped down to the substrate.

III. PROBLEM STATEMENT

This article studies a simple but challenging task in robotic folding: creating a predefined crease on a sheet of paper of typical geometry (e.g., rectangular, diamond, etc.) as is illustrated in Fig. 2. Only one end of the paper is manipulated while the other end is left free. Thus, extra fixtures are unnecessary and the folding task can be completed by a single manipulator, which simplifies the workspace, but slippage of the paper against the substrate must be mitigated during manipulation, which is a challenge.

The task can be divided into two sub-tasks and three states. The first sub-task is manipulating one end of the paper from the initial flat state (Fig. 2(a)) to the folding state (Fig. 2(b)), with the goal that the manipulated edge or point should overlap precisely with the crease target line or point C as shown in the figure. With the manipulated edge of the paper at the origin, the manipulator moves in the x direction. Since the manipulated paper usually has relatively high bending stiffness, large nonlinear elastic deformations are induced in the folding state. In the second sub-task, the paper must be permanently deformed to form the desired crease at $C/2$, thus achieving the final folded state (Fig. 2(c)).

IV. PHYSICS-BASED MODEL AND ANALYSIS

We next present the numerical framework for studying the underlying physics of the paper folding process. First, we analyze the main deformations of the manipulated paper and prove that a 2D model is sufficient to learn the behaviors of the manipulated paper so long as the sheet is symmetrical. Second, we briefly introduce a physically accurate numerical model based on prior work in computer graphics [44]. Third, we formulate a generalized strategy for paper folding using scaling analysis.

A. Reduced-Order Model Representation

Paper is a unique deformable object. Unlike cloth, its surface is developable [45]; i.e., the surface can bend but not stretch. Furthermore, shear deformations are not of particular importance as the geometry of the manipulated paper is symmetrical. Therefore, the primary nonlinear deformation when folding paper in our scenario is bending deformation. We

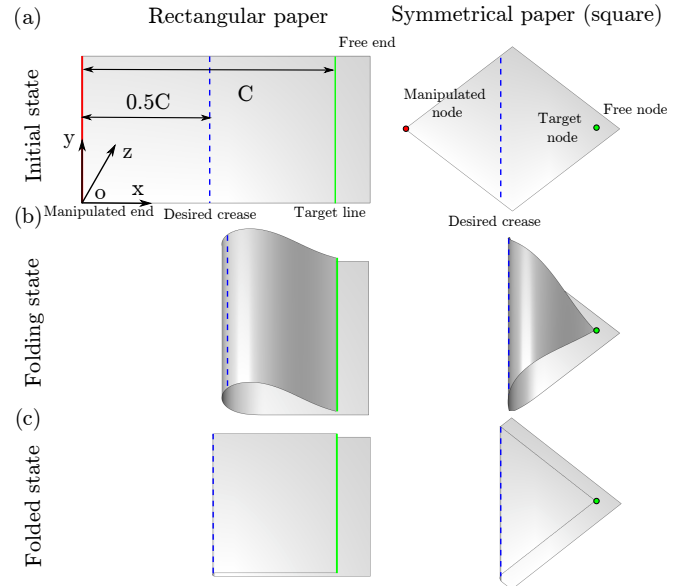


Fig. 2. Folding sheets of paper. The manipulation process involves (a) the initial state, where the paper lies flat on the substrate, followed by (b) the folding state, where the manipulated end is moved to the “crease target” line C , and finally (c) the folded state, which involves forming the desired crease on the paper.

postulate that the nonlinear behaviors of paper arise primarily from a balance of bending and gravitational energies: $\epsilon_b \sim \epsilon_g$.

To further understand the energy balance of the manipulated paper, we analyze an arbitrary piece in the paper, as shown in Fig. 3(b). The bending energy of this piece can be written as

$$\epsilon_b = \frac{1}{2} k_b \kappa^2 l, \quad (1)$$

where l is its undeformed length of the piece, κ is its curvature, and its bending stiffness is

$$k_b = \frac{1}{12} Ewh^3, \quad (2)$$

where w is its undeformed width, h is its thickness, and E is its Young’s modulus. The gravitational energy of the piece is

$$\epsilon_g = \rho whlgH, \quad (3)$$

where ρ is its volume density and H is its vertical height above the rigid substrate.

From the above equations, we obtain a characteristic length called the gravito-bending length, which encapsulates the influence of bending and gravity:

$$L_{gb} = \left(\frac{Eh^2}{24\rho g} \right)^{\frac{1}{3}} \sim \left(\frac{h}{\kappa^2} \right)^{\frac{1}{3}}. \quad (4)$$

The length is in units of meters, and we can observe that it scales proportionally to the ratio of thickness to curvature squared, which are the key quantities describing the deformed configuration of the manipulated paper. Note that the formulation of L_{gb} contains only one geometric parameter, the paper thickness h , which means that other geometric quantities (i.e., length l and width w) have no influence on the deformed configuration.

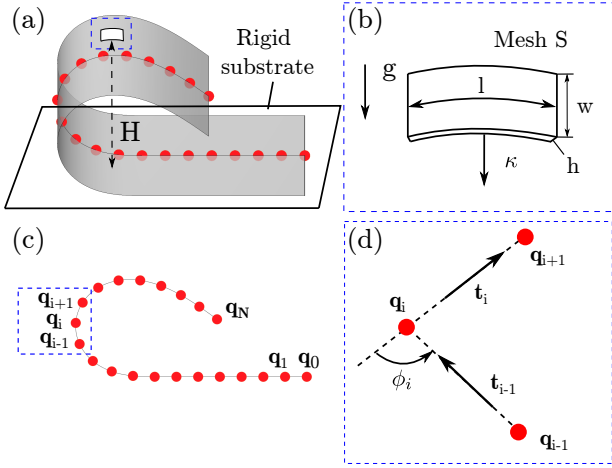


Fig. 3. (a) Schematic of a paper during the folding state. (b) Bending deformations of a small piece in the paper. (c) Reduced-order discrete model (planar rod) representation of our paper. (d) Notations in the discrete model.

Additionally, due to the symmetrical geometry of the paper, curvature κ should be identical for all regions at the same height H . Therefore, we can simply use the centerline of the paper, as shown in Fig. 3(a), to express the paper’s configuration. We model this centerline as a 2D planar rod since deformations are limited to the x, z plane. We implement a discrete-differential-geometry (DDG)-based numerical simulation to simulate the 2D planar rod. We present the details of this numerical framework in the next section.

B. Discrete Differential Geometry Numerical Model

Following pioneering work on physics-based modeling and simulation of deformable curves, surfaces, and solids [46]–[48], the computer graphics community has shown impressive results using DDG-based simulation frameworks. For example, the Discrete Elastic Rods (DER) [44] framework has shown efficient and physically accurate simulation of deformable linear objects in various scenarios including knot tying [49], helix bifurcations [50], coiling of rods [51], and flagella buckling [52]. Given this success, we use DER to model the centerline of the paper as a 2D planar rod undergoing bending deformations.

As shown in Fig. 3(c), the discrete model is comprised of $N + 1$ nodes, \mathbf{q}_i ($0 \leq i \leq N$). Each node, \mathbf{q}_i , represents two degrees of freedom (DOF): position along the x and the z axes. This results in a $2N + 2$ -sized DOF vector representing the configuration of the sheet, $\mathbf{q} = [\mathbf{q}_0, \mathbf{q}_1, \dots, \mathbf{q}_N]^T$, where T is the transpose operator. Initially, all the nodes of the paper are located in a line along the x -axis in the paper’s undeformed state. As the robotic manipulator imposes boundary conditions on the end node \mathbf{q}_N , portions of the paper deform against the substrate as shown in Fig. 4(a). We compute the DOFs as a function of time $\mathbf{q}(t)$ by integrating the equations of motion (EOM) at each DOF.

Before describing the EOM, we first outline the elastic energies of the rod as a function of \mathbf{q} . Kirchhoff’s rod theory tells us that the elastic energies of a rod can be divided into

stretching E_s , bending E_b , and twisting E_t energies. First, The stretching elastic energy is

$$E_s = \frac{1}{2} k_s \sum_{i=0}^{N-1} \left(1 - \frac{\|\mathbf{q}_{i+1} - \mathbf{q}_i\|}{\Delta l} \right)^2 \Delta l, \quad (5)$$

where $k_s = EA$ is the stretching stiffness; E is Young’s modulus; $A = wh$ is the cross-sectional area, and Δl is the undeformed length of each edge (segment between two nodes). The bending energy is

$$E_b = \frac{1}{2} k_b \sum_{i=2}^{N-1} \left(2 \tan \frac{\phi_i}{2} - 2 \tan \frac{\phi_i^0}{2} \right)^2 \frac{1}{\Delta l}, \quad (6)$$

where $k_b = \frac{Ewh^3}{12}$ is the bending stiffness; w and h are the width and thickness respectively; ϕ_i is the “turning angle” at a node as shown in Fig. 3(d), and ϕ_i^0 is the undeformed turning angle (0 for paper). Finally, since we limit our system to a 2D plane, we can forgo twisting energies entirely. The total elastic energy is then simply $E_{el} = E_s + E_b$.

Indeed, a ratio $k_s/k_b \sim w/h^2 \gg 1$ indicates that stretching strains will be minimal which matches our intuition as paper is usually easy to bend but not stretch. Therefore, the stretching energy item in (5) acts as a constraint to prevent obvious stretching for the modeled planar rod.

We can now construct our EOM as a simple force balance

$$\mathcal{P}(\mathbf{q}) \equiv \mathbb{M}\dot{\mathbf{q}} + \frac{\partial E_{el}}{\partial \mathbf{q}} - \mathbf{F}^{\text{ext}} = 0, \quad (7)$$

where \mathbb{M} is the diagonal lumped mass matrix; $\dot{(\)}$ represents derivatives with respect to time; $-\frac{\partial E_{el}}{\partial \mathbf{q}}$ is the elastic force vector, and \mathbf{F}^{ext} is the external forces applied on the paper. Note that (7) can be solved using Newton’s method, allowing for full simulation of the 2D planar rod under manipulation.

C. Generalized Solution and Scaling Analysis

As mentioned in Sec. III, the core of the folding task is to manipulate the end \mathbf{q}_N to the target position C starting from an initially flat state shown in Fig. 4(a). To do so, we analyze the physical system in order to achieve a solution capable of minimizing sliding during manipulation.

We first denote several quantities to describe the deformed configuration of the paper. Here, we introduce a point \mathbf{q}_C , which is the node that connects the suspended ($z > 0$) and unsuspended regions ($z = 0$) of the paper. We focus primarily on the suspended region as deformations occur solely in this region. An origin \mathbf{o} is defined for our 2D plane which is located at the initial manipulated end \mathbf{q}_N as shown in Fig. 4(a). For the manipulated end, the robot end-effector imposes a position $\mathbf{q}_N = (x, z)$ and an orientation angle α to control the pose of the manipulated end as shown in Fig. 4(a). On the connective node \mathbf{q}_C , the tangent is always along the x -director. Here, we impose a constraint that the curvature at the manipulated end is always zero so that sharp bending deformations are prevented, which is crucial to preventing permanent deformations during

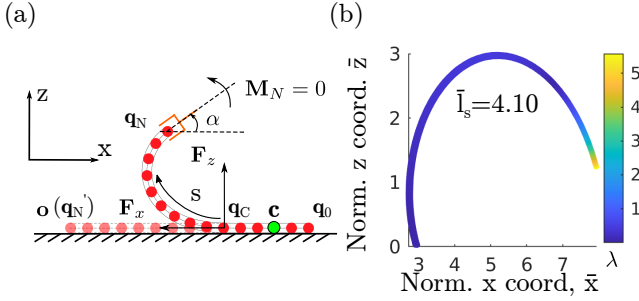


Fig. 4. (a) Side view of a symmetrical paper during folding with coordinate frame and relevant notations. (b) Sampled λ forces for a particular \bar{l}_s of 4.10. This showcases one of the sampled “partial” force manifolds that we use train our neural network on.

the folding process. With these definitions, we can now modify (7) with the following constraints:

$$\begin{aligned} \mathcal{P}(\mathbf{q}) &= 0, \\ \text{s.t. } \mathbf{q}_N &= (x, z), \\ \frac{d\mathbf{q}_C}{ds} &= (-1, 0), \\ M_N &= 0, \\ l_s &\equiv \int_{\mathbf{q}_C}^{\mathbf{q}_N} ds = \mathbf{q}_C \cdot \hat{\mathbf{x}}, \end{aligned} \quad (8)$$

where M_N is the external moment applied on the manipulated end; s is the arc length of the paper’s centerline, and l_s is the arc length of the suspended region (from \mathbf{q}_C to \mathbf{q}_N).

We can solve (8) with the numerical framework presented in Sec. IV-B resulting in a unique DOF vector \mathbf{q} . Note that when \mathbf{q} is determined, we can then obtain the external forces from the substrate along the paper $\mathbf{F}_{\text{substrate}} = \mathbf{F}_x + \mathbf{F}_z$, orientation angle α of the manipulated end, and the suspended length l_s . Recall that through (4), Young’s modulus E , thickness h , and density ρ were determined to be the main material and geometric properties of the paper. Therefore, we can outline the following physical relationship relating all our quantities:

$$\begin{aligned} \lambda &= \frac{\|\mathbf{F}_x\|}{\|\mathbf{F}_z\|}, \\ (\lambda, \alpha, l_s) &= f(E, h, \rho, x, z), \end{aligned} \quad (9)$$

where f is an unknown relationship. It is then trivial to see that to prevent sliding the relationship

$$\lambda \leq \mu_s \quad (10)$$

must be satisfied, where μ_s is the static friction coefficient between the paper and the substrate. Therefore, a trajectory that minimizes sliding is one that minimizes λ along its path.

One glaring problem remains in that the relation f must be known to generate any sort of trajectory. In the absence of an analytical solution, the numerical framework from Sec. IV-B can be used to exhaustively find mappings between the inputs and outputs of f . However, generating tuples in this fashion requires solving the high-dimensional problem in (8). Such a method would be horribly inefficient and would make real-time operation infeasible. Instead, we opt to obtain an analytical

approximation of f by fitting a neural network on simulation data. Currently, this approach has several shortcomings. For one, directly learning f is difficult given that (9) currently depends on five parameters as input, resulting in a high dimensional relationship. Furthermore, since the formulation directly depends on intrinsic parameters of the paper (E , ρ , and h), an enormously exhaustive range of simulations must be run to gather enough data to accurately learn f .

To solve all the aforementioned shortcomings, we reduce the dimensionality of the problem by applying scaling analysis. According to Buckingham π theorem, we construct five dimensionless groups: $\bar{x} = x/L_{gb}$; $\bar{z} = z/L_{gb}$; $\bar{l}_s = l_s/L_{gb}$; α , and $\lambda = F_t/F_n$, where L_{gb} is the gravito-bending length from (4). This results in a non-dimensionalized formulation of (9) which is expressed as

$$(\lambda, \alpha, \bar{l}_s) = \mathcal{F}(\bar{x}, \bar{z}). \quad (11)$$

Note that the mapping relationship \mathcal{F} is now irrelevant to quantities with units, e.g., material and geometric properties of the paper. As the dimensionality of our problem has been reduced significantly, we can now express λ as a function of just two parameters \bar{x}, \bar{z} . Therefore, training a neural network to model \mathcal{F} is now trivial as non-dimensionalized simulation data from a single type of paper can be used. Furthermore, the low dimensionality of \mathcal{F} allows us easily visualize the λ landscape along a non-dimensional 2D-plane. In the next section, we will now go over the steps to model \mathcal{F} .

V. DEEP LEARNING AND OPTIMIZATION

A. Data Generation

In order to learn the force manifold, we solve (8) for several sampled (x, z) points. An example of the partial force manifold produced from this sampling can be observed for a single suspended length in Fig. 4(b). For a specific (x, z) location, we apply incremental rotations along the y-axis and find the optimal rotation angle α that results in $M_N = 0$ on the manipulated end. For a particular configuration (x, z, α) , we then record the suspended length l_s as well as the tangential and normal forces experienced on the clamped end. This leads to a training dataset \mathcal{D} consisting of six element tuples $(F_t, F_n, \alpha, l_s, x, z)$. We then non-dimensionalize this dataset to the form $(\lambda, \alpha, \bar{l}_s, \bar{x}, \bar{z})$. A total of 95796 training samples were used within a normalized suspended length of $\bar{l}_s \leq 6.84$, which adequately includes the workspace of most papers.

B. Learning Force and Optimal Grasp Orientation

We can now train on our dataset \mathcal{D} to obtain a generalized neural network modeling \mathcal{F} :

$$(\lambda, \alpha, \bar{l}_s) = \mathcal{F}_{\text{NN}}(\bar{x}, \bar{z}). \quad (12)$$

To obtain the above function, a simple fully-connected feed-forward nonlinear regression network is trained with 4 hidden layers, each containing 392 nodes. Aside from the final output layer, each layer is followed by a rectified linear unit (ReLU) activation. In addition, we preprocess all inputs through the standardization

$$\mathbf{x}' = \frac{\mathbf{x} - \bar{\mathbf{x}}_{\mathcal{D}}}{\sigma_{\mathcal{D}}}, \quad (13)$$

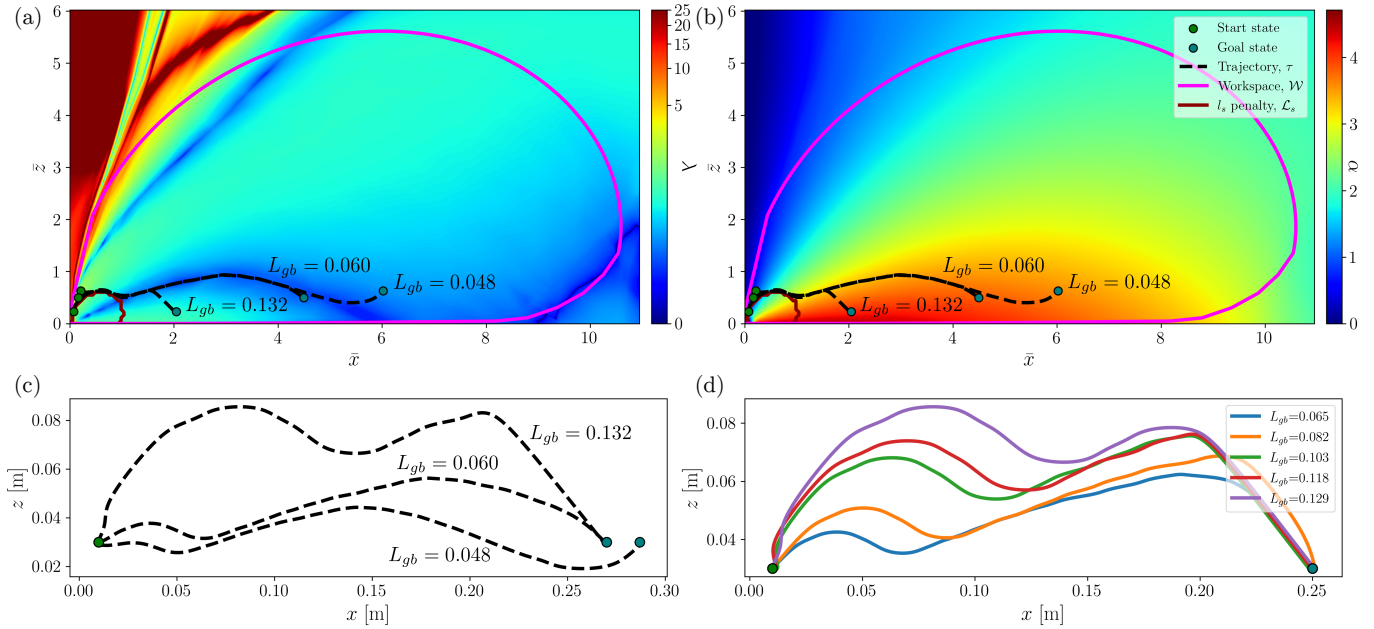


Fig. 5. (a) Visualization of the trained neural network’s non-dimensionalized λ force manifold \mathcal{M} and (b) α manifold. An extremely low $\bar{\delta}$ discretization is used to showcase smoothness. For the force manifold, we observe two distinctive local minima canyons. Note that regions outside the workspace \mathcal{W} are physically inaccurate but are of no consequence to us as they are ignored. For the α manifold, we observe continuous smooth interpolation all throughout which is key for producing feasible trajectories. Both manifolds showcase the used trajectories in the experiments for folding paper in half for $L_{gb} \in [0.048, 0.060, 0.132]$. (c) Showcases the three trajectories in (a) and (b) scaled back to real space. These are the actual trajectories used by the robot. (d) Arbitrary trajectories for various L_{gb} with identical start and goal states are shown to highlight the effect of the material property on our control policy.

where \mathbf{x} is the original input, $\bar{\mathbf{x}}_{\mathcal{D}}$ is the mean of the dataset \mathcal{D} , and $\sigma_{\mathcal{D}}$ is the standard deviation of \mathcal{D} .

We use an initial 80-20 train-val split on the dataset \mathcal{D} with a batch size of 128. Mean absolute error (MAE) is used as the error. We alternate between stochastic gradient descent (SGD) and Adam whenever training stalls. Furthermore, we gradually increase the batch size up to 4096 and train on the entire dataset once MAE reaches < 0.001 . Using this scheme, we achieve an MAE of < 0.0005 .

C. Constructing the Neural Force Manifold

The neural force manifold (i.e. λ outputs of \mathcal{F}_{NN} for the workspace set) is discretized into a rectangular grid consisting of $\bar{\delta} \times \bar{\delta}$ blocks, where $\bar{\delta} = \delta/L_{gb}$. For each of the blocks, we obtain and store a single λ value using the midpoint of the block. This results in a discretized neural force manifold \mathcal{M} represented as a $m \times n$ matrix. For the purposes of path planning, we add two components to our manifold. First, we do not allow exploration into any region not belonging to our dataset distribution ($\bar{l}_s > 6.84$). We do so by defining a workspace \mathcal{W} as all (\bar{x}, \bar{z}) pairs within the concave hull of the input portion of the dataset \mathcal{D} . Secondly, we also exclude regions within a certain \bar{l}_s threshold. This is done as positions with small suspended lengths and large α angles may result in high curvatures that could cause collision with our gripper and/or plastic deformation, both of which we wish to avoid. We denote this region as the penalty region \mathcal{L}_s . A visualization of \mathcal{M} with the workspace \mathcal{W} and penalty boundary \mathcal{L}_s regions can be seen in Fig. 5(a). The α values corresponding to the manifold are also shown in Fig. 5(b).

D. Path Planning over the Neural Force Manifold

Given the discretized manifold \mathcal{M} , we can now generate optimal trajectories through traditional path planning algorithms. We define an optimal trajectory τ^* as one that gets to the goal state while minimizing the sum of λ :

$$\tau^* = \arg \min_{\tau \in \mathcal{T}} \sum_{i=0}^{L-1} \lambda_i, \quad (14)$$

where L is the length of the trajectory and \mathcal{T} is the set of all valid trajectories from the desired start to goal state. We define a valid trajectory as one that is contained within the acceptable region

$$(x_i, z_i) \in \mathcal{W} \setminus \mathcal{L}_s \quad \forall (x_i, z_i) \in \tau,$$

and whose consecutive states are adjacent grid locations. Given the discretization of the NFM, we can treat \mathcal{M} as a graph whose edge weights consist of λ . Therefore, we can use uniform cost search to obtain τ^* . The pseudocode of the path planning algorithm can be seen in Alg. 1.

VI. ROBOTIC SYSTEM

A. Dual Manipulator Setup

For our experiments, we use two Rethink Robotics’ Sawyer manipulators as shown in Fig. 7. One arm has an elongated gripper designed for folding, while the other arm has a spring compliant roller for creasing and an Intel Realsense D435 camera for vision feedback. The elongated gripper has rubber attached to the insides of the fingers for tight gripping.

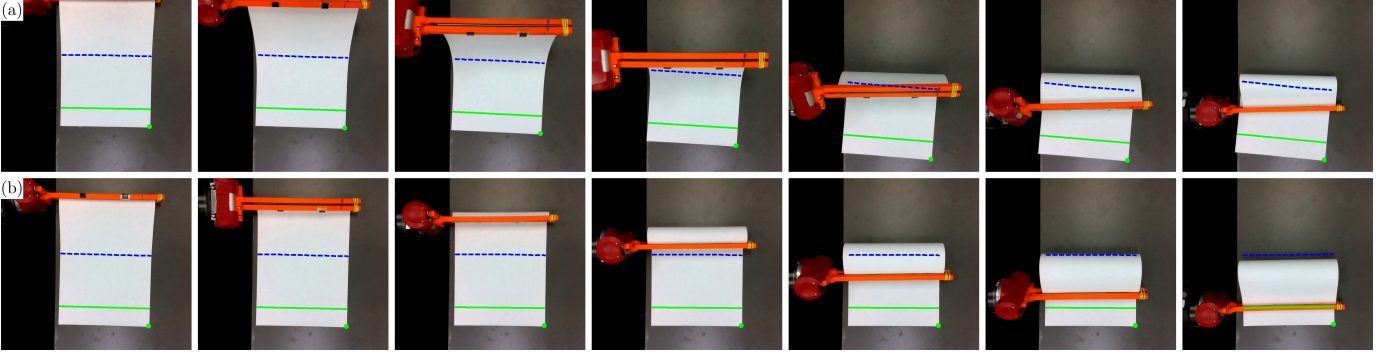


Fig. 6. Example of our perception system with a top down view of the folding procedure. (a) Showcases the the intuitive baseline results while (b) showcases our open-loop algorithm for $L_{gb} = 0.048$ and $C = 0.25\text{m}$. Similar to Fig. 2, the solid green line indicates the desired end effector position while the dashed blue line indicates the crease location. We observe that the intuitive baseline has considerable sliding while our open-loop algorithm has near-perfect performance for this case.

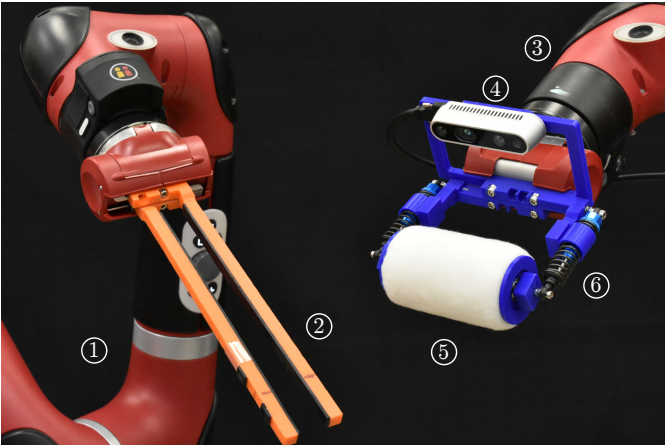


Fig. 7. Experimental apparatus: Two robot manipulators, one for folding (1) and the other for creasing (3). An elongated gripper (2) is used for grabbing the manipulated end of the folding paper. A roller (5) with compliant springs (6) is used for forming the crease. An Intel RealSense D435 camera (4) is attached to the creasing arm offer vision feedback during the folding procedure. All gripper attachments were 3D printed.

B. Perception System

For our perception, we take an eye-in-hand approach by attaching an Intel Realsense D435 to the roller arm. We do not use the depth component of the camera as we align the camera to be pointing down along the world z -axis and the distance from the camera to the table is known. To detect the pose of the paper, we use simple color detection to segment the paper and then use Shi-Tomasi corner detection [53] to obtain the position of the bottom edge. An example of the top-down view as well as detected poses produced by the camera can be seen in Fig. 6.

C. Vision-feedback Control

Although we minimize λ with our proposed framework, sliding could still happen due to a substrate's low friction surface and/or jittering of the robot's end-effector. Notice that the generated optimal trajectory τ^* from Sec. V-D assumes that the origin \mathbf{o} of our coordinate system shown in Fig. 4(a) is fixed. We can define the origin as $\mathbf{o} = \mathbf{q}_0 - L\hat{\mathbf{x}}$ where

Algorithm 1: Uniform Cost Search

Input: $\bar{x}_s, \bar{z}_s, \bar{x}_g, \bar{z}_g, \mathcal{M}$
Output: τ^*

```

1 Func UCS ( $\bar{x}_s, \bar{z}_s, \bar{x}_g, \bar{z}_g, \mathcal{M}$ ):
2    $\mathcal{W} \leftarrow$  valid workspace of  $\mathcal{M}$ 
3    $\mathcal{L}_s \leftarrow l_s$  penalty region
4    $\mathbf{h} \leftarrow$  initialize min heap priority queue
5    $\mathbf{c} \leftarrow$  initialize empty list
6    $n_s \leftarrow$  node with location  $(\bar{x}_s, \bar{z}_s)$  and cost 0
7    $n_g \leftarrow$  node with location  $(\bar{x}_g, \bar{z}_g)$  and cost 0
8    $\mathbf{h}.push(n_s)$ 
9   while  $\text{len}(\mathbf{h}) > 0$  do
10     $n_i \leftarrow \mathbf{h}.pop()$ 
11    if  $n_i == n_g$  then
12       $\tau^* \leftarrow$  path from start to goal
13      break
14     $\mathbf{c}.append(n_i)$ 
15    for  $(\bar{x}_j, \bar{z}_j) \in$  neighbors of  $n_i$  do
16      if  $(\bar{x}_j, \bar{z}_j) \notin \mathcal{W} \setminus \mathcal{L}_s$  then
17        continue
18       $n_j \leftarrow$  node with location  $(\bar{x}_j, \bar{z}_j)$  and cost
19         $\lambda_j$  from  $\mathcal{M}$ 
20      if  $n_j \in \mathbf{c}$  then
21        continue
22      if  $n_j \in \mathbf{h}$  and cost of  $n_j$  is higher then
23        continue
24       $\mathbf{h}.push(n_j)$ 
25   $\tau^* \leftarrow$  perform trajectory smoothing on  $\tau^*$ 
return  $\tau^*$ 

```

L is the total length of the paper. Any amount of sliding indicates that \mathbf{q}_0 is moving along the x -axis and therefore, the origin \mathbf{o} also moves an identical amount. When this occurs, our position within the manifold during traversal deviates from the optimal trajectory. Furthermore, without adaptive replanning, the amount of sliding Δx will directly result in Δx amount of error when creasing. To circumvent this, we introduce a vision-feedback approach that mitigates the effects of sliding.

We perform vision-feedback at N evenly spaced out intervals

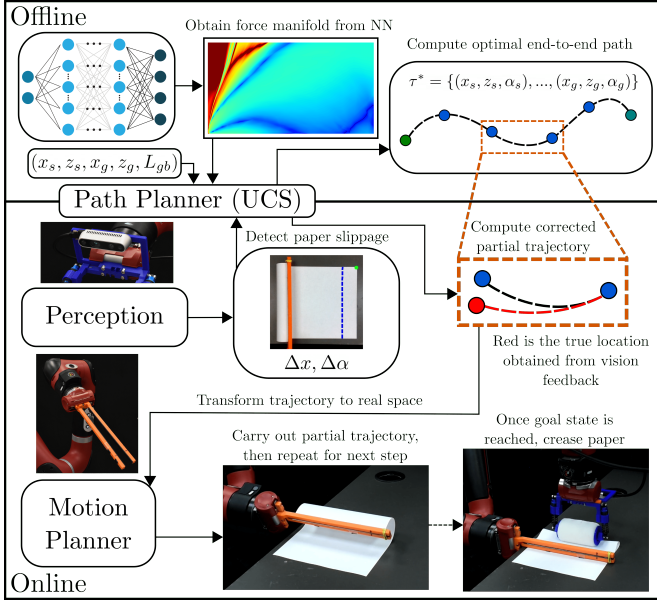


Fig. 8. An overview of our folding pipeline. The top row showcases offline proponents while the bottom row shows online. On the offline side, we use our trained neural network to generate the necessary force manifold for planning. Then, given an input tuple $(x_s, z_s, x_g, z_g, L_{gb})$, we generate an end-to-end trajectory using uniform cost search. This end-to-end trajectory is then split up into partial trajectories that are carried out by the robot. At the conclusion of each partial trajectory, we measure paper sliding and replan the next partial trajectory to rectify the error.

of the trajectory τ^* as shown in Fig. 8. To do so, we first split up τ^* into N partial trajectories. Aside from the first partial trajectory τ_0^* , we extract the start and goal states of the other $1 \leq i \leq N$ partial trajectories resulting in a sequence of N evenly spaced out states $\mathcal{S} = \{(x_1, z_1, \alpha_1), \dots, (x_N, z_N, \alpha_N)\}$ when accounting for overlaps. After carrying out τ_0^* , we detect the amount of sliding Δx and incorporate this error by updating the start state and non-dimensionalizing as

$$\bar{x}_i^c = \frac{x_i - \Delta x}{L_{gb}}.$$

We then replan a partial trajectory τ_i^* from the updated start state (x_i^c, z_i) to the next state (x_{i+1}, z_{i+1}) in the sequence and carry out this updated trajectory. This is repeated until reaching the goal state. By properly accounting for sliding, we ensure that the traversal through the NFM is as accurate as possible. We note that this scheme allows us obtain corrected partial trajectories in near real time once N becomes sufficiently large as each partial trajectory's goal state becomes increasingly close to its start state, allowing for uniform cost search to conclude rapidly. We direct the reader to the supplementary videos mentioned in Sec. I which showcase the speed of the feedback loop.

Rectifying the sliding Δx is not the only error we must address. Recount that we assume an optimal grasp orientation α for each position within the manifold. When the origin of our NFM moves, our true position does not match the intended position, resulting in also an angular error

$$\begin{aligned} \alpha_i^c &= \mathcal{F}_{\text{NN}}(\bar{x}_i^c, \bar{z}_i), \\ \Delta \alpha &= \alpha_i - \alpha_i^c. \end{aligned}$$

Algorithm 2: Closed-loop Control Pseudocode

Input: $(x_s, z_s), (x_g, z_g), L_{gb}, \delta, N, \mathcal{F}_{\text{NN}}$

- 1 $\mathcal{M} \leftarrow \text{DiscretizeManifold}(\mathcal{F}_{\text{NN}}, \delta)$
- 2 $\bar{x}_s, \bar{z}_s, \bar{x}_g, \bar{z}_g \leftarrow \text{non-dimensionalize with } L_{gb}$
- 3 $\bar{\tau}^* \leftarrow \text{UCS}(\bar{x}_s, \bar{z}_s, \bar{x}_g, \bar{z}_g, \mathcal{M})$
- 4 update $\bar{\tau}^*$ with α_s using \mathcal{F}_{NN}
- 5 $\tau^* \leftarrow \text{convert } \bar{\tau}^* \text{ to real space with } L_{gb}$
- 6 $\tau_0^*, \dots, \tau_{N-1}^* \leftarrow \text{SplitTrajectory}(\tau^*, N)$
- 7 $\mathcal{S} \leftarrow \text{extract start and goal states}$
- 8 carry out τ_0^* on robot
- 9 **for** (x_i, z_i, α_i) and $(x_{i+1}, z_{i+1}, \alpha_{i+1}) \in \mathcal{S}$ **do**
- 10 $\Delta x \leftarrow \text{detect sliding of paper}$
- 11 $x_i^c \leftarrow x_i - \Delta x$
- 12 $\bar{x}_i^c, \bar{z}_i, \bar{x}_{i+1}, \bar{z}_{i+1} \leftarrow \text{non-dimensionalize with } L_{gb}$
- 13 $\alpha_i^c \leftarrow \mathcal{F}_{\text{NN}}(\bar{x}_i^c, \bar{z}_i)$
- 14 $\Delta \alpha \leftarrow \alpha_i - \alpha_i^c$
- 15 $\bar{\tau}_i^* \leftarrow \text{UCS}(\bar{x}_i^c, \bar{z}_i, \bar{x}_{i+1}, \bar{z}_{i+1}, \mathcal{M})$
- 16 $L \leftarrow \text{len}(\bar{\tau}_i^*)$
- 17 $\alpha_i \leftarrow \text{obtain } \alpha \text{ of } \bar{\tau}_i^* \text{ using } \mathcal{F}_{\text{NN}}$
- 18 $\alpha_i^c \leftarrow \alpha_i + \Delta \alpha [1, (L-1)/L, \dots, 1/L, 0]^T$
- 19 append $\bar{\tau}_i^*$ with α_i^c
- 20 $\tau_i^* \leftarrow \text{convert } \bar{\tau}_i^* \text{ to real space with } L_{gb}$
- 21 carry out τ_i^* on robot
- 22 crease paper with roller

Simply applying a $-\Delta \alpha$ update to the first point in a partial trajectory results in a large rotational jump that only exacerbate the sliding issue. Furthermore, we postulate that so long as sliding is not extremely large, the incorrect α at the current position within the manifold is still fairly optimal. Therefore, the $\Delta \alpha$ error is incorporated to the trajectory gradually:

$$\begin{aligned} \tau_i^* &= \text{UCS}(\bar{x}_i^c, \bar{z}_i, \bar{x}_{i+1}, \bar{z}_{i+1}, \mathcal{M}), \\ \alpha_i &= \mathcal{F}_{\text{NN}}(\tau_i^*), \\ \alpha_i^c &= \alpha_i + \Delta \alpha [1, (L-1)/L, \dots, 1/L, 0]^T, \end{aligned}$$

where UCS stands for uniform cost search and L is the length of the trajectory τ_i^* . This gradual correction ensures that we minimize sliding while maintaining smoothness of the trajectory. The pseudocode for our full closed-loop algorithm can be seen in Alg. 2.

VII. EXPERIMENTS AND ANALYSIS

A. Measuring the Material Property of Paper

To use our framework, we must develop a way to accurately measure the parameter L_{gb} for a particular piece of paper. As mentioned previously, L_{gb} encapsulates the influence of bending and gravity. With this in mind, we propose a simple way to measure the parameter.

As shown in Fig. 10(a), when one end of the paper is fixed, the paper will deform due to the coupling of bending

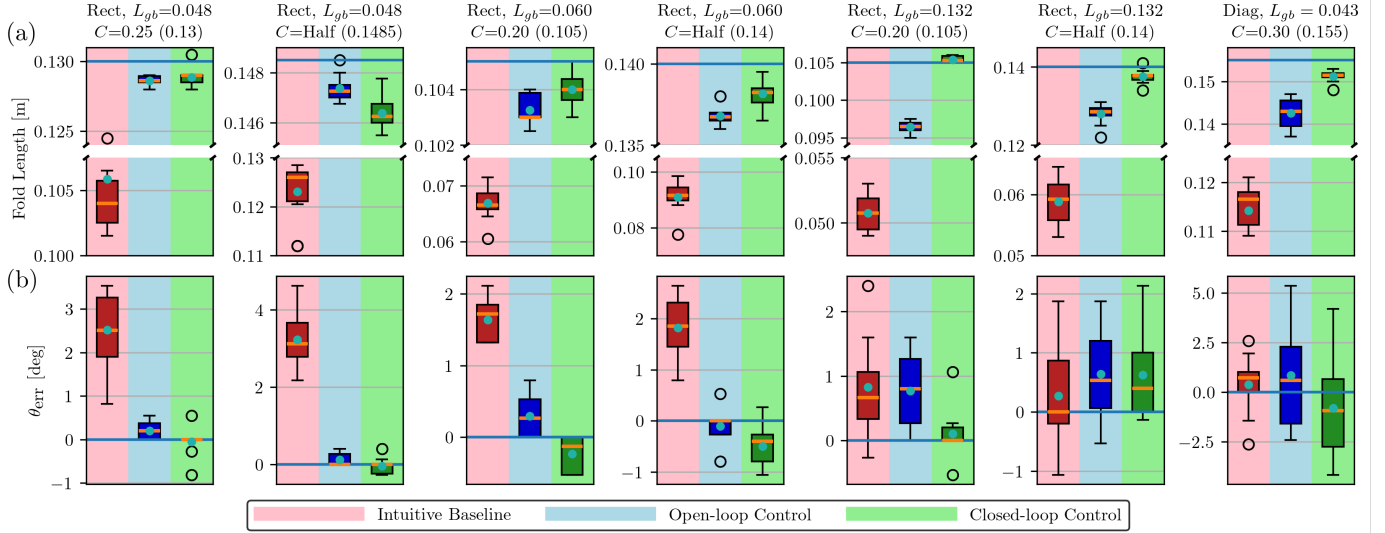


Fig. 9. Experimental results for all folding scenarios. Each column indicates a folding scenario while the top row (a) showcases the fold length and bottom row (b) showcases the spin error. Boxplot results are shown color coded for the intuitive baseline, open-loop control, and closed-loop control algorithms. Medians are shown as orange lines, means are shown as turquoise circles, and the desired target value is shown as a light blue horizontal line. We note that both our open-loop and closed-loop algorithms have significant improvements over the intuitive baseline as shown by the broken axis in (a). Our algorithms also have significantly less variance.

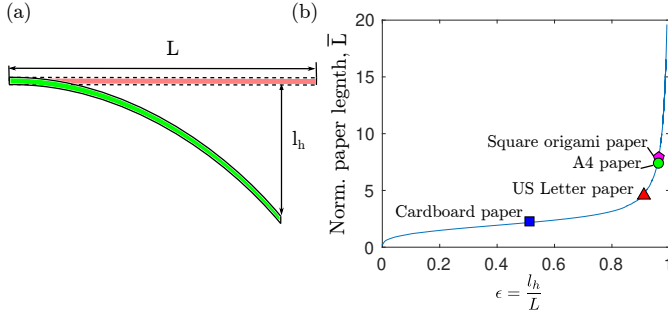


Fig. 10. (a) Schematic of a hanging plate. The manipulation edge is fixed horizontally; (b) Relationship between the ratio $\epsilon = l_h/L$ and normalized total length of the paper $\bar{L} = L/L_{gb}$.

and gravitational energy. Therefore, the following mapping relationship exists:

$$\begin{aligned} \bar{L} &= \mathcal{L}(\epsilon), \\ \bar{L} &= \frac{L}{L_{gb}}, \\ \epsilon &= \frac{l_h}{L}, \end{aligned} \quad (15)$$

where l_h is the vertical distance from the free end to the fixed end and L is the total length of the paper. We can obtain the mapping relationship $\mathcal{L}(\epsilon)$ using numerical simulations, which is shown in Fig. 10(b). With this mapping known, simple algebra can be performed to obtain L_{gb} . First, we measure the ratio $\epsilon = l_h/L$ for a particular paper to obtain its corresponding normalized total length \bar{L} . Then, the value of L_{gb} can be calculated simply by $L_{gb} = L/\bar{L}$. Once we obtain L_{gb} , we can now use the non-dimensionalized mapping relationship in (11) to find the optimal path for manipulating the paper.

B. Experimental Setup

For our experiments, we tested folding on 4 distinct types of paper:

- 1) A4 paper, $L_{gb} = 0.048\text{m}$,
- 2) US Letter paper, $L_{gb} = 0.060\text{m}$,
- 3) Cardboard paper (US Letter dimensions), $L_{gb} = 0.132\text{m}$,
- 4) Square origami paper, $L_{gb} = 0.043\text{m}$.

For the rectangular papers (1-3), we do two sets of experiments. The first involves folding the papers to an arbitrary crease location ($C = 0.25\text{m}$ for A4 and $C = 0.20\text{m}$ for US Letter and cardboard), while the second involves folding the papers in half. For the square origami paper, we choose an arbitrary crease location of $C = 0.30\text{m}$. This results in a total of 7 folding scenarios. For each of the scenarios, we conduct experiments using 3 different algorithms (an intuitive baseline, our open-loop approach, and our closed-loop approach). We complete 10 trials for each of these algorithms, resulting in a total of 210 experiments.

C. Baseline Algorithm

To showcase the benefits of our folding algorithm, we compare our algorithm to an intuitive baseline. We can think of an intuitive baseline algorithm as one that would work if the opposite end of the paper were fixed to the substrate. Naturally, such a trajectory would be one that grabs the edge of the paper and traces the half perimeter of a circle with radius $R = C/2$:

$$\begin{aligned} d\theta &= \pi/M, \\ \tau_B &= \{(R \cos(id\theta), R \sin(id\theta), id\theta) \forall i \in [0, M]\}, \end{aligned} \quad (16)$$

where M is an arbitrary number of points used as the resolution of trajectory. We choose $M = 250$ for all experiments.

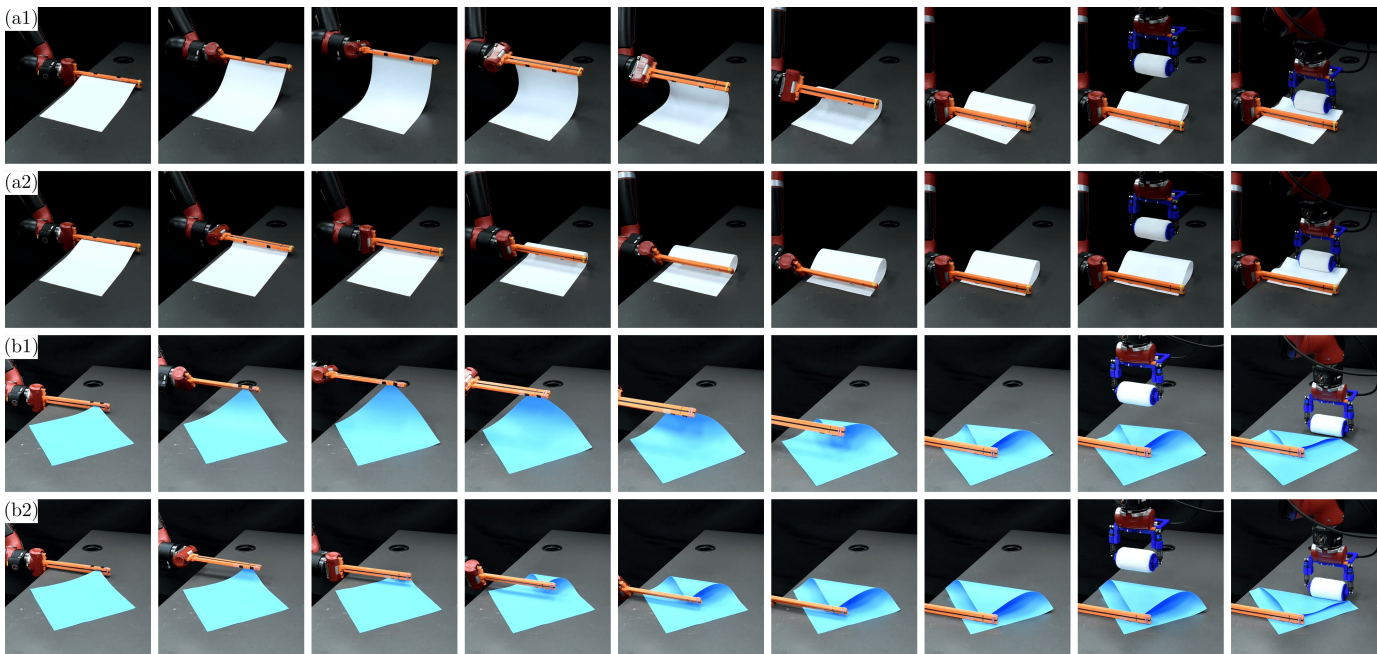


Fig. 11. Isometric views of different folding scenarios. (a1-2) showcases $C = \text{Half}$ folding for $L_{gb} = 0.048$ paper with the intuitive baseline and our open-loop algorithm, respectively. (b1-2) showcases $C = 0.30\text{m}$ diagonal folding for $L_{gb} = 0.043$ with the intuitive baseline our closed-loop algorithm, respectively.

D. Metrics

The metrics used for the experiments were the average fold length and the spin error. The average fold length was calculated by simply taking the average of the left and right side lengths up until the crease. The spin error was calculated as the angle θ_{err} that results in the difference between the left and right side lengths. For square papers, the fold length was defined as the perpendicular length from the tip to the crease and the spin error was the angular deviation from this line to the true diagonal.

E. Parameters

The neural force manifold \mathcal{M} was discretized using a $\bar{\delta}$ corresponding to $\delta = 2\text{mm}$ depending on the material as we found this discretization to have good compromise between accuracy and computational speed. All rectangular papers used a penalty region \mathcal{L}_s defined by $\bar{l}_s < 0.958$ while the square paper used one defined by $\bar{l}_s < 1.137$. This discrepancy is due to the fact that the diagonal paper has a smaller yield strength compared to the rectangular paper, i.e., to prevent extremely high curvatures, a larger suspended length \bar{l}_s range must be avoided.

For closed-loop control, we chose to split all trajectories into $N = 5$ intervals regardless of trajectory length. Furthermore, we use an extremely slick (i.e. low friction) table to showcase the robustness of our method. Using an empirical method, we measured the static coefficient of friction of our papers and the substrate to be approximately $\mu_s = 0.12$. For comparison, the static coefficient of friction for steel on steel (both lubricated with castor oil) is $\mu_s = 0.15$.

F. Results and Analysis

All experimental results can be seen expressed as box plots where we showcase achieved fold lengths and spin errors in Fig. 9(a) and (b), respectively. When observing the achieved fold lengths, we see significant improvement over the baseline for all folding scenarios. Due to the large gap in performance, broken axes are used to properly display the variance of the recorded data. We note that not only do our algorithms achieve significantly better performance on average, the variance of our approaches is also much lower as shown by the decreased y-axis resolution after the axis break. We attribute the high variance of the baseline method due to the increased influence of friction, which can often cause chaotic, unpredictable results. In other words, truly deterministic folding can only be achieved when sliding is nonexistent.

For a vast majority of cases, we observe a clear improvement over the open-loop algorithm when incorporating vision-feedback. Intuitively, we observe a trend where the performance gap between our open-loop and closed-loop algorithms grow as the material stiffness increases for rectangular folding. For softer materials ($L_{gb} = 0.048$), the open-loop algorithm has near perfect performance as shown when folding a paper in half in Fig. 11(a2). In comparison, Fig. 11(a1) showcases the baseline algorithm failing with significant sliding.

The sliding problem is only exacerbated by increasing the stiffness of the material ($L_{gb} = 0.132$) where Fig. 12(a) showcases the baseline algorithm failing to fold the cardboard paper in half by a margin almost as long as the paper itself. In comparison, our open-loop algorithm is capable of folding the cardboard with significantly better results albeit with some visual sliding as shown in Fig. 12(b). As the material stiffness increases, the benefits of the incorporated vision-feedback are more clearly seen as we are able to achieve near perfect

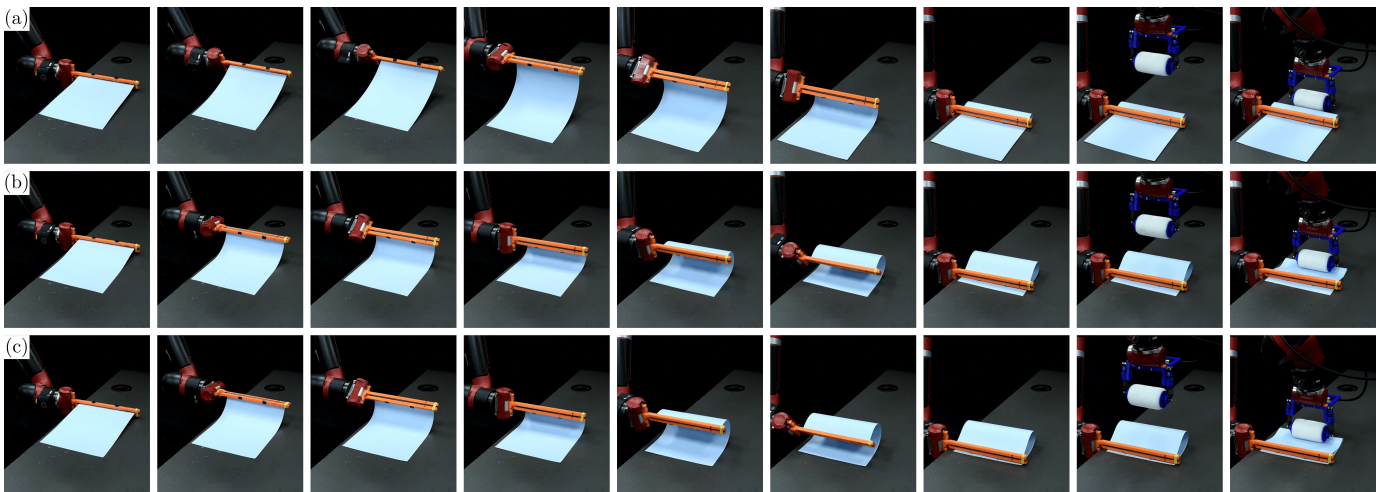


Fig. 12. Isometric views for folding $C = \text{Half}$ with the stiffest paper ($L_{gb} = 0.132$). (a) showcases the intuitive baseline, which fails drastically as the stiffness of the paper causes excessive sliding during the folding process. (b) showcases our open-loop algorithm, which has significant improvements over the baseline with minimal sliding. Finally, (c) showcases our closed-loop algorithm, which improves upon our open-loop results and achieves near perfect folding.

folding for cardboard in Fig. 12(c). All of our findings for rectangular folding also match the results of our diagonal folding experiment shown in Fig. 11(b1-b2), where closed-loop once again achieves minimal sliding when compared to the baseline. Overall, the matching findings across all of our experiments showcase the robustness of our formulation against material and geometric factors.

We observe one oddity for the folding scenario of $L_{gb} = 0.048$ and $C = \text{Half}$ where the open-loop algorithm outperformed our closed-loop variant. Still, we wish to point out that this decrease in performance is only on average 1mm, which can easily be attributed to repetitive discretization error caused by $N = 5$ replanning. In fact, as we use a discretization of $\delta = 2\text{mm}$ for the manifold, compounding rounding errors can easily cause 1-2mm errors. With this in mind, our closed-loop method achieves an average fold length performance within a 1-2mm tolerance across all experiments.

In terms of spin error, we found that softer materials had the greatest error. As the frictional surface of the table is not perfectly even, any amount of sliding will directly result in uneven spin as shown in Fig. 11(a). As the material stiffness increases, the spin errors became more uniform across the methods as the influence of friction is not enough to deform the paper. Still, we can see that our open and closed-loop algorithms had less sliding than the baseline on average.

VIII. CONCLUSION

We have introduced a novel control strategy capable of robustly folding sheets of paper of varying materials and geometries with only a single manipulator. Our framework incorporates a combination of techniques spanning several disciplines, including physical simulation, machine learning, scaling analysis, and path planning. The effectiveness of our framework was showcased through extensive real world experiments against an intuitive baseline. Furthermore, an efficient near real-time visual-feedback algorithm was implemented that further minimizes folding error. With our closed-loop sensorimotor control algorithm successfully accomplished

challenging scenarios such as folding stiff cardboard with repeatable accuracy.

For future work, we hope to tackle the difficult problem of creating arbitrary creases along sheets of paper with non-symmetric centerlines. Such non-symmetric papers can no longer be represented as a reduced-order model of a 2D elastic rod, thus requiring a different formulation. Additionally, folding along regions of paper with preexisting creases will also be a crucial step to achieving elegant folding tasks such as robotic origami. Moving forward, we anticipate exploring solutions to such problems that take advantage of generalized problem formulations with data-driven control schemes such as reinforcement learning.

We acknowledge financial support from the National Science Foundation under Grant numbers IIS-1925360, CAREER-2047663, and OAC-2209782.

REFERENCES

- [1] M. C. Gemici and A. Saxena, "Learning haptic representation for manipulating deformable food objects," in *2014 IEEE/RSJ International Conference on Intelligent Robots and Systems*, pp. 638–645, IEEE, 2014.
- [2] P. Long, W. Khalil, and P. Martinet, "Force/vision control for robotic cutting of soft materials," in *2014 IEEE/RSJ International Conference on Intelligent Robots and Systems*, pp. 4716–4721, IEEE, 2014.
- [3] H. Kang and J. T. Wen, "Endobot: a robotic assistant in minimally invasive surgeries," in *Proceedings 2001 ICRA. IEEE International Conference on Robotics and Automation (Cat. No. 01CH37164)*, vol. 2, pp. 2031–2036, IEEE, 2001.
- [4] N. Haouchine, W. Kuang, S. Cotin, and M. Yip, "Vision-based force feedback estimation for robot-assisted surgery using instrument-constrained biomechanical three-dimensional maps," *IEEE Robotics and Automation Letters*, vol. 3, no. 3, pp. 2160–2165, 2018.
- [5] I. Leizea, A. Mendizabal, H. Alvarez, I. Aguinaga, D. Borro, and E. Sanchez, "Real-time visual tracking of deformable objects in robot-assisted surgery," *IEEE computer graphics and applications*, vol. 37, no. 1, pp. 56–68, 2015.
- [6] A. Kapusta, Z. Erickson, H. M. Clever, W. Yu, C. K. Liu, G. Turk, and C. C. Kemp, "Personalized collaborative plans for robot-assisted dressing via optimization and simulation," *Autonomous Robots*, vol. 43, no. 8, pp. 2183–2207, 2019.
- [7] A. Clegg, W. Yu, J. Tan, C. K. Liu, and G. Turk, "Learning to dress: Synthesizing human dressing motion via deep reinforcement learning," *ACM Transactions on Graphics (TOG)*, vol. 37, no. 6, pp. 1–10, 2018.

- [8] W. Yu, A. Kapusta, J. Tan, C. C. Kemp, G. Turk, and C. K. Liu, "Haptic simulation for robot-assisted dressing," in *2017 IEEE international conference on robotics and automation (ICRA)*, pp. 6044–6051, IEEE, 2017.
- [9] Z. Erickson, H. M. Clever, G. Turk, C. K. Liu, and C. C. Kemp, "Deep haptic model predictive control for robot-assisted dressing," in *2018 IEEE international conference on robotics and automation (ICRA)*, pp. 4437–4444, IEEE, 2018.
- [10] E. Pignat and S. Calinon, "Learning adaptive dressing assistance from human demonstration," *Robotics and Autonomous Systems*, vol. 93, pp. 61–75, 2017.
- [11] T. L. Chen, M. Ciocarlie, S. Cousins, P. M. Grice, K. Hawkins, K. Hsiao, C. C. Kemp, C.-H. King, D. A. Lazewatsky, A. E. Leeper, et al., "Robots for humanity: using assistive robotics to empower people with disabilities," *IEEE Robotics & Automation Magazine*, vol. 20, no. 1, pp. 30–39, 2013.
- [12] T. Bhattacharjee, G. Lee, H. Song, and S. S. Srinivasa, "Towards robotic feeding: Role of haptics in fork-based food manipulation," *IEEE Robotics and Automation Letters*, vol. 4, no. 2, pp. 1485–1492, 2019.
- [13] Y. Kita, F. Kanehiro, T. Ueshiba, and N. Kita, "Clothes handling based on recognition by strategic observation," in *2011 11th IEEE-RAS International Conference on Humanoid Robots*, pp. 53–58, IEEE, 2011.
- [14] A. Doumanoglou, J. Stria, G. Peleka, I. Mariolis, V. Petrik, A. Kargakos, L. Wagner, V. Hlaváč, T.-K. Kim, and S. Malassiotis, "Folding clothes autonomously: A complete pipeline," *IEEE Transactions on Robotics*, vol. 32, no. 6, pp. 1461–1478, 2016.
- [15] M. Cusumano-Towner, A. Singh, S. Miller, J. F. O'Brien, and P. Abbeel, "Bringing clothing into desired configurations with limited perception," in *2011 IEEE international conference on robotics and automation*, pp. 3893–3900, IEEE, 2011.
- [16] J. Maitin-Shepard, M. Cusumano-Towner, J. Lei, and P. Abbeel, "Cloth grasp point detection based on multiple-view geometric cues with application to robotic towel folding," in *2010 IEEE International Conference on Robotics and Automation*, pp. 2308–2315, IEEE, 2010.
- [17] L. Twardon and H. Ritter, "Interaction skills for a coat-check robot: Identifying and handling the boundary components of clothes," in *2015 IEEE International Conference on Robotics and Automation (ICRA)*, pp. 3682–3688, IEEE, 2015.
- [18] A. Doumanoglou, A. Kargakos, T.-K. Kim, and S. Malassiotis, "Autonomous active recognition and unfolding of clothes using random decision forests and probabilistic planning," in *2014 IEEE international conference on robotics and automation (ICRA)*, pp. 987–993, IEEE, 2014.
- [19] J. Schulman, A. Gupta, S. Venkatesan, M. Tayson-Frederick, and P. Abbeel, "A case study of trajectory transfer through non-rigid registration for a simplified suturing scenario," in *2013 IEEE/RSJ International Conference on Intelligent Robots and Systems*, pp. 4111–4117, IEEE, 2013.
- [20] W. H. Lui and A. Saxena, "Tangled: Learning to untangle ropes with rgb-d perception," in *2013 IEEE/RSJ International Conference on Intelligent Robots and Systems*, pp. 837–844, IEEE, 2013.
- [21] W. Wang, D. Berenson, and D. Balkcom, "An online method for tight-tolerance insertion tasks for string and rope," in *2015 IEEE International Conference on Robotics and Automation (ICRA)*, pp. 2488–2495, IEEE, 2015.
- [22] Y. Yamakawa, A. Namiki, and M. Ishikawa, "Simple model and deformation control of a flexible rope using constant, high-speed motion of a robot arm," in *2012 IEEE International Conference on Robotics and Automation*, pp. 2249–2254, IEEE, 2012.
- [23] A. Nair, D. Chen, P. Agrawal, P. Isola, P. Abbeel, J. Malik, and S. Levine, "Combining self-supervised learning and imitation for vision-based rope manipulation," in *2017 IEEE international conference on robotics and automation (ICRA)*, pp. 2146–2153, IEEE, 2017.
- [24] S. Kudoh, T. Gomi, R. Katano, T. Tomizawa, and T. Suehiro, "In-air knotting of rope by a dual-arm multi-finger robot," in *2015 IEEE/RSJ International Conference on Intelligent Robots and Systems (IROS)*, pp. 6202–6207, IEEE, 2015.
- [25] Y. Yamakawa, A. Namiki, and M. Ishikawa, "Motion planning for dynamic knotting of a flexible rope with a high-speed robot arm," in *2010 IEEE/RSJ International Conference on Intelligent Robots and Systems*, pp. 49–54, IEEE, 2010.
- [26] J. Matas, S. James, and A. J. Davison, "Sim-to-real reinforcement learning for deformable object manipulation," in *Conference on Robot Learning*, pp. 734–743, PMLR, 2018.
- [27] D. McConachie and D. Berenson, "Estimating model utility for deformable object manipulation using multiarmed bandit methods," *IEEE Transactions on Automation Science and Engineering*, vol. 15, no. 3, pp. 967–979, 2018.
- [28] X. Lin, Y. Wang, J. Olkin, and D. Held, "Softgym: Benchmarking deep reinforcement learning for deformable object manipulation," *arXiv preprint arXiv:2011.07215*, 2020.
- [29] H. K. H. Kim, D. Bourne, S. Gupta, and S. S. Krishnan, "Automated process planning for robotic sheet metal bending operations," *Journal of Manufacturing Systems*, vol. 17, pp. 338 – 360, September 1998.
- [30] D. J. Balkcom and M. T. Mason, "Robotic origami folding," *The International Journal of Robotics Research*, vol. 27, no. 5, pp. 613–627, 2008.
- [31] S. Müller, J. van den Berg, M. Fritz, T. Darrell, K. Goldberg, and P. Abbeel, "A geometric approach to robotic laundry folding," *The International Journal of Robotics Research*, vol. 31, no. 2, pp. 249–267, 2012.
- [32] A. X. Lee, H. Lu, A. Gupta, S. Levine, and P. Abbeel, "Learning force-based manipulation of deformable objects from multiple demonstrations," in *2015 IEEE International Conference on Robotics and Automation (ICRA)*, pp. 177–184, IEEE, 2015.
- [33] A. X. Lee, A. Gupta, H. Lu, S. Levine, and P. Abbeel, "Learning from multiple demonstrations using trajectory-aware non-rigid registration with applications to deformable object manipulation," in *2015 IEEE/RSJ International Conference on Intelligent Robots and Systems (IROS)*, pp. 5265–5272, 2015.
- [34] M. Rambow, T. Schauß, M. Buss, and S. Hirche, "Autonomous manipulation of deformable objects based on teleoperated demonstrations," in *2012 IEEE/RSJ International Conference on Intelligent Robots and Systems*, pp. 2809–2814, IEEE, 2012.
- [35] P.-C. Yang, K. Sasaki, K. Suzuki, K. Kase, S. Sugano, and T. Ogata, "Repeatable folding task by humanoid robot worker using deep learning," *IEEE Robotics and Automation Letters*, vol. 2, no. 2, pp. 397–403, 2017.
- [36] V. Petrík and V. Kyrki, "Feedback-based fabric strip folding," in *2019 IEEE/RSJ International Conference on Intelligent Robots and Systems (IROS)*, pp. 773–778, 2019.
- [37] Y. Zheng, F. F. Veiga, J. Peters, and V. J. Santos, "Autonomous learning of page flipping movements via tactile feedback," *IEEE Transactions on Robotics*, 2022.
- [38] W. Yan, A. Vangipuram, P. Abbeel, and L. Pinto, "Learning predictive representations for deformable objects using contrastive estimation," *arXiv preprint arXiv:2003.05436*, 2020.
- [39] V. Petrík, V. Smutný, P. Krsek, V. Hlaváč, "Physics-based model of a rectangular garment for robotic folding," in *2016 IEEE/RSJ International Conference on Intelligent Robots and Systems (IROS)*, pp. 951–956, 2016.
- [40] V. Petrík, V. Smutný, and V. Kyrki, "Static stability of robotic fabric strip folding," *IEEE/ASME Transactions on Mechatronics*, vol. 25, no. 5, pp. 2493–2500, 2020.
- [41] Y. Li, Y. Yue, D. Xu, E. Grinspun, and P. K. Allen, "Folding deformable objects using predictive simulation and trajectory optimization," in *2015 IEEE/RSJ International Conference on Intelligent Robots and Systems (IROS)*, pp. 6000–6006, 2015.
- [42] C. Elbrechter, R. Haschke, and H. Ritter, "Folding paper with anthropomorphic robot hands using real-time physics-based modeling," in *2012 12th IEEE-RAS International Conference on Humanoid Robots (Humanoids 2012)*, pp. 210–215, IEEE, 2012.
- [43] A. Namiki and S. Yokosawa, "Robotic origami folding with dynamic motion primitives," in *2015 IEEE/RSJ International Conference on Intelligent Robots and Systems (IROS)*, pp. 5623–5628, IEEE, 2015.
- [44] M. Bergou, M. Wardetzky, S. Robinson, B. Audoly, and E. Grinspun, "Discrete elastic rods," in *ACM SIGGRAPH 2008 Papers*, SIGGRAPH '08, (New York, NY, USA), Association for Computing Machinery, 2008.
- [45] D. Hilbert and S. Cohn-Vossen, *Geometry and the Imagination*, vol. 87. American Mathematical Soc., 2021.
- [46] D. Terzopoulos, J. Platt, A. Barr, and K. Fleischer, "Elastically deformable models," in *Proceedings of the 14th Annual Conference on Computer Graphics and Interactive Techniques (ACM SIGGRAPH 87)*, pp. 205–214, 1987.
- [47] D. Terzopoulos and K. Fleischer, "Modeling inelastic deformation: Viscoelasticity, plasticity, fracture," in *Proceedings of the 15th Annual Conference on Computer Graphics and Interactive Techniques (ACM SIGGRAPH 88)*, pp. 269–278, 1988.
- [48] D. Terzopoulos and K. Fleischer, "Deformable models," *The Visual Computer*, vol. 4, no. 6, pp. 306–331, 1988.
- [49] A. Choi, D. Tong, M. K. Jawed, and J. Joo, "Implicit contact model for discrete elastic rods in knot tying," *Journal of Applied Mechanics*, vol. 88, no. 5, 2021.
- [50] D. Tong, A. Borum, and M. K. Jawed, "Automated stability testing of elastic rods with helical centerlines using a robotic system," *IEEE Robotics and Automation Letters*, vol. 7, no. 2, pp. 1126–1133, 2021.

- [51] M. K. Jawed, F. Da, J. Joo, E. Grinspun, and P. M. Reis, "Coiling of elastic rods on rigid substrates," *Proceedings of the National Academy of Sciences*, vol. 111, no. 41, pp. 14663–14668, 2014.
- [52] D. Tong, A. Choi, J. Joo, and M. K. Jawed, "A fully implicit method for robust frictional contact handling in elastic rods," *arXiv preprint arXiv:2205.10309*, 2022.
- [53] J. Shi and Tomasi, "Good features to track," in *1994 Proceedings of IEEE Conference on Computer Vision and Pattern Recognition*, pp. 593–600, 1994.